

Asymmetrical regulation of thermal transport in BAs/MoSSe van der Waals heterostructures with applied electric field

Donghai Wei ¹, E Zhou,¹ Jinyuan Xu,¹ Ailing Chen,¹ Hanpeng Xie,¹ Fuqing Duan,¹ Huimin Wang ², Zhenzhen Qin ³, and Guangzhao Qin ^{1,*}

¹State Key Laboratory of Advanced Design and Manufacturing Technology for Vehicle, College of Mechanical and Vehicle Engineering, Hunan University, Changsha 410082, People's Republic of China

²Hunan Key Laboratory for Micro-Nano Energy Materials & Device and School of Physics and Optoelectronics, Xiangtan University, Xiangtan 411105, Hunan, China

³Key Laboratory of Materials Physics, Ministry of Education, School of Physics, Zhengzhou University, Zhengzhou 450001, China



(Received 3 September 2023; accepted 4 April 2024; published 6 May 2024)

As a nondestructive regulation method, applying external electric field to regulate thermal transport has become one of the most effective reversible strategies. However, to date, using external electric fields to regulate thermal transport in *van der Waals* (vdW) heterostructures has been rarely reported, despite the great significance to engineering heat-transfer applications in electronics. Herein, based on the *state-of-the-art* first-principles calculations, we investigate the external electric field engineered thermal transport in BAs/MoSSe vdW twins heterostructures (i.e., BAs/MoSSe-I and BAs/MoSSe-II), which are constructed from monolayer BAs and Janus MoSSe. The thermal conductivity of different stacked BAs/MoSSe shows similar response to positive electric field. However, with negative electric field applied, the thermal conductivity of BAs/MoSSe-II is 22.4 times higher than that of BAs/MoSSe-I under the strength of -0.2 V \AA^{-1} . Detailed analysis reveals that the renormalization of phonons driven by the electric field mainly affects the phonon anharmonicity, which is induced by the electric field enhanced or weakened interlayer interaction, finally leading to the different response of the thermal conductivity for the two stacked BAs/MoSSe. The highly effective regulation of thermal transport in vdW heterostructures driven by the external electric fields as shown in this study is valuable for physical and engineering applications in electronics, thermoelectric, and thermal management.

DOI: [10.1103/PhysRevB.109.205408](https://doi.org/10.1103/PhysRevB.109.205408)

I. INTRODUCTION

Two-dimensional (2D) van der Waals (vdW) heterostructures have shown great appeal for the novel physical and chemical properties beyond original monolayer structures, which have been widely promoted in optoelectronics [1–3], nanoelectronics [4,5], catalysis [6,7], and also extended to the fundamental photodetectors [8,9], tunneling devices [1,10,11], memory device [8,12,13], etc. Undoubtedly, regulating the thermal transport properties of heterostructures induced by the weak vdW interface is of great physical significance and engineering application values. Generally, enhancing the *in-plane* thermal transport properties can effectively mitigate the Joule heat generated during the carrier transport process, which ultimately improves the lifetime and reliability of electronic devices. Conversely, the reduction in thermal transport properties can significantly improve the energy conversion efficiency of thermoelectric materials and extend industrial applications in the thermal insulating equipment [14,15].

Previous studies have shown that the intrinsic thermal conductivity of materials can be effectively regulated by structural engineering, such as strain, doping, defects, etc. [16–23].

However, the traditional structural modulation strategies usually rely on the modification of the material itself, which undoubtedly places a noticeable burden on the materials. Besides, the actual service lifetime of the materials under the structural modulation strategies also suffers from great challenges. Compared to the structural modulation strategy as mentioned above, the external electric field modulation method, distinguished by its reversibility and nondestructiveness, has been widely explored for improving the electronic, optical, and phononic performances of 2D materials in recent years [24–30]. For instance, Wang *et al.* reported that the type-II band alignment of the ZnO/MoSSe heterostructures can be tuned to type-I and type-III band alignment by applying the external electric fields [31]. Specifically, the regulation of electric field applied to thermal transport can be traced back to the group of Hopkins and co-workers in 2015. By manipulating the ferroelastic domain of the $\text{Pb}(\text{Zr}_{0.3}\text{Ti}_{0.7})\text{O}_3$ thin films with electric field, its thermal conductivity lowered by 11% compared with the pristine one [32], which experimentally verifies the effectiveness of electric field on heat-transport regulation. Additionally, our previous work theoretically predicted the regulation of electric field on the thermal transport with silicene as a study case [33], whereafter, the electric field is widely applied in the research of 2D borophene, InSe, GaN, germanene, bilayer graphene, etc. [34–38]. However, the regulation of electric field on thermal transport properties

*Corresponding author: gzqin@hnu.edu.cn

is currently limited to single-species materials. As a matter of fact, interfacial thermal transport induced by different materials is a practical problem that cannot be negligible. Thus, exploring the effect of external electric field on the thermal transport properties of heterostructures is of great practical application value, especially for 2D vdW heterostructures.

Janus monolayer group-VI chalcogenides XMN ($X = \text{Mo}, \text{W}, \text{Cr}, \text{Zr}, \text{etc.}$; M and $N = \text{S}, \text{Se}, \text{Te}$) with MoSSe as a representative have attracted much attention for their unique asymmetric sandwich structure and fantastic properties. Previous studies confirm that these 2D Janus materials demonstrate excellent band adjustability [39,40], piezoelectricity [41–43], ferroelectricity [44], Rashba effect [45–47], etc. Additionally, BAs as a representative direct semiconductor with high thermal conductivity [48,49], ultrahigh carrier mobility, as well as the dynamical stability, has also received enormous attention [50–52]. Thus, it would be of great significance to physical and engineering applications to explore the thermal transport properties together with the response to the external electric fields of twins' vdW heterostructures result from the different arrangements derived from monolayer BAs and Janus MoSSe.

In this paper, combining the superior physical and chemical properties of monolayer BAs and Janus MoSSe, we construct two types of twins' heterostructures (BAs/MoSSe-I and BAs/MoSSe-II), where the thermal transport properties are investigated systematically by applying external electric field. The result shows that the response of the thermal conductivity to the external electric field is different for different stacking sequences of the twins' heterostructures. Detailed analysis is conducted from the interlayer charge distribution driven by the external electric field, followed by the modulated interatomic interaction, which leads to the phonon renormalization and finally affects the phonon anharmonicity, resulting in the regulated thermal transport properties. The modulated thermal transport properties of BAs/MoSSe twins' heterostructures by external electric field shown in this paper provide an effective method for tuning the thermal conductivity of the 2D vdW heterostructures and greatly expand the application prospects of 2D materials.

II. METHODS

All the density-functional theory (DFT) calculations are performed using projector augmented-wave method in the Vienna *Ab initio* Simulation Package (VASP) [53–55]; the Perdew-Burke-Ernzerhof (PBE) of the generalized gradient approximation [56] is selected for describing exchange-correlation functional with the energy and forces converged to 10^{-6} eV and 10^{-8} eV \AA^{-1} , respectively. A Monkhorst-Pack [57] k mesh of $15 \times 15 \times 1$ is used to sample the first Brillouin zone. Dipole sheets are set in the middle of the vacuum regions in the VASP package to simulate the out-of-plane electric field. Herein, the vacuum layer along the out of plane is set as 25 \AA to avoid the interaction being affected by periodicity. The dipole moment correction is also considered with each external electric field during the geometry optimization as well as the following calculations. The optB86b is adopted to accurately describe the vdW interactions between BAs and MoSSe layers.

The harmonic and anharmonic interatomic force constants (IFCs) can be obtained by the finite displacement difference method applied in PHONOPY [58] and THIRDORDER.PY [59] package, respectively. A $4 \times 4 \times 1$ supercell including 100 atoms and a $2 \times 2 \times 1$ k mesh is adopted based on the optimized configurations. The phonon dispersions can be extracted after diagonalizing the harmonic dynamical matrix. Considering the sensibility of the thermal conductivity to the atom neighbors, the sixth-nearest neighboring atoms of anharmonic IFCs are adopted after the fine test of the thermal conductivity for the two stackings. Combining with the harmonic, anharmonic IFCs, and the essential control files including the Born effective charge and dielectric constant to take into account the long-range electrostatic interaction, the SHENGBTE [59] package is employed to obtain the thermal conductivity of the materials by solving the phonon Boltzmann transport equation (BTE). To evaluate the size-dependent thermal transport properties, the phonon boundary scattering due to finite size is considered, which can be estimated by the equation

$$\left(\frac{1}{\tau_\lambda}\right)_{\text{boundary}} = \frac{1-p}{1+p} \frac{|v_\lambda|}{L}, \quad (2)$$

where p is the specularly parameter, which means the fraction of specularly scattered phonons depending on the roughness of the edge, ranging from 0 to 1, where the p is set to 0 for a completely rough edge to consider the boundary scattering, v_λ is the phonon group velocity of the phonon mode λ , and L is the sample size usually ranging from nanometers to micrometers. The temperature gradient is assumed to be along the direction of the finite sample length. Then, the scattering rate of each phonon mode is calculated by the Matthiessen rule:

$$\frac{1}{\tau_\lambda} = \left(\frac{1}{\tau_\lambda}\right)_{\text{anharmonic}} + \left(\frac{1}{\tau_\lambda}\right)_{\text{isotopic}} + \left(\frac{1}{\tau_\lambda}\right)_{\text{boundary}}. \quad (3)$$

In this work, considering the relative intrinsic low thermal conductivity of the BAs/MoSSe twins' heterostructures, only three-phonon scattering interactions are considered for the total calculations. Thus, the data in the study can be obtained through the postprocessing script.

III. RESULTS

In consideration of the unique *out-of-plane* asymmetric monolayer structure of Janus-MoSSe, twins' heterostructures based on monolayer BAs and MoSSe are theoretically constructed as shown in Figs. 1(a) and 1(b) named as BAs/MoSSe-I and BAs/MoSSe-II, respectively. The S atoms are close to the BAs plane in BAs/MoSSe-I, while Se atoms for BAs/MoSSe-II. The direction of the external electric field is shown by the yellow gradient arrow inset in Figs. 1(a) and 1(b). The planar average of the electrostatic potential along the *out-of-plane* direction is shown in Supplemental Material, Fig. S1 [60]. The electrostatic potential gradient from BAs layer to the MoSSe layer further confirms the structural differences for BAs/MoSSe-I and BAs/MoSSe-II. The electrostatic potential-energy difference can be found on the side of the S (Se) atom layer and B atom layer, which result from the different charge accumulation, caused by the different

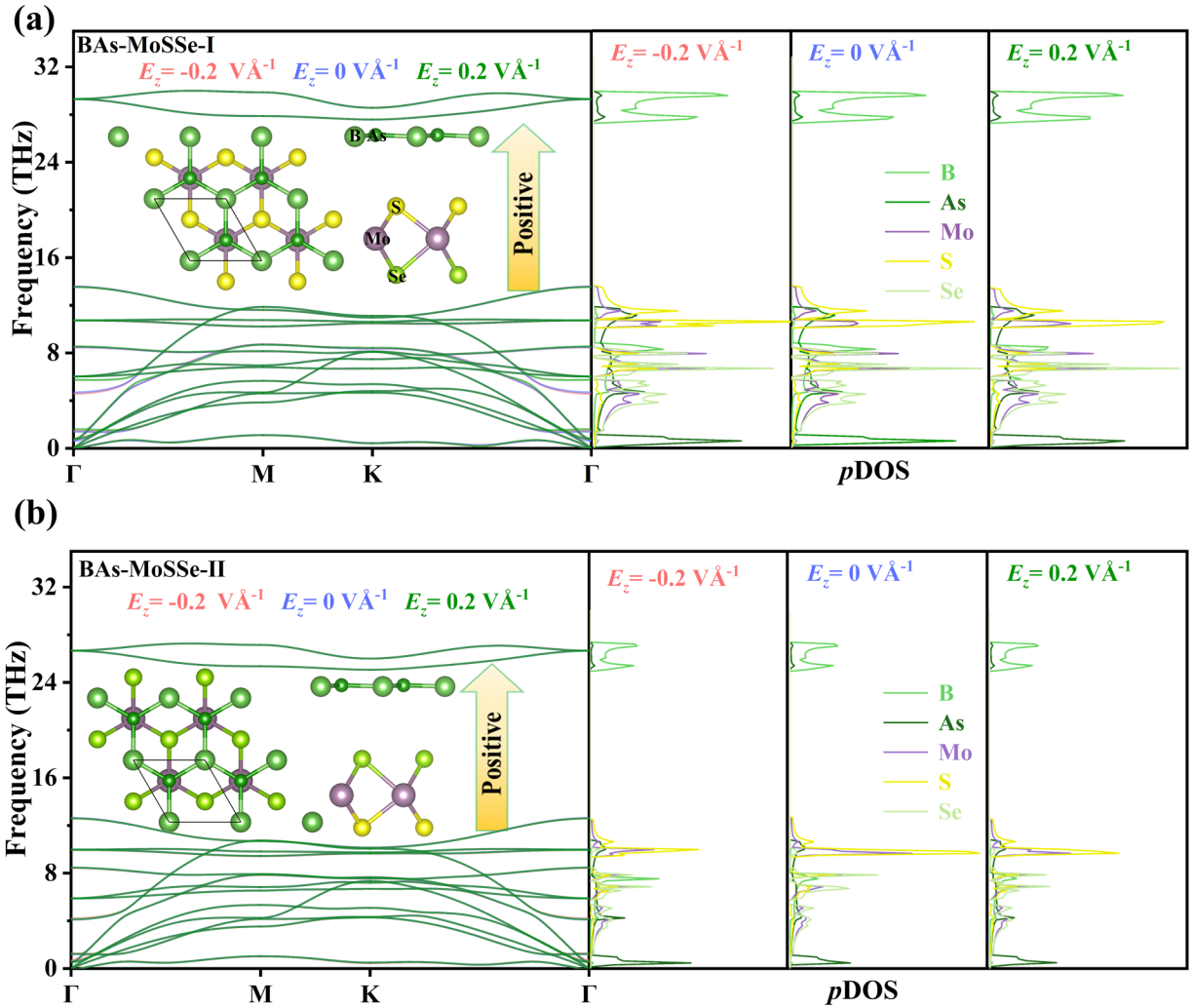


FIG. 1. The phonon spectrum along the high-symmetry path of $\Gamma - M - K - \Gamma$ and the partial density of states ($pDOS$) of (a) BAAs/MoSSe-I and (b) BAAs/MoSSe-II under the representative external electric fields ($E_z = 0, \pm 0.2 \text{ V \AA}^{-1}$). (Inset: three views of the crystal structure; the large pale green, small bottle green, yellow, purple, and grass-green balls represent B, As, S, Mo, and Se atoms, respectively, and the external electric fields are marked by the yellow gradient arrow along the out of plane.)

electronegativity between S and Se atoms, and finally lead to the different work functions of BAAs/MoSSe-I ($\Delta\phi = 0.47 \text{ eV}$) and BAAs/MoSSe-II ($\Delta\phi = 0.93 \text{ eV}$). Additionally, the result of the work function, which illustrates a proportional relationship with the dipole moment according to the Helmholtz equation, is in good agreement with the discussion of the dipole moment to be analyzed as follows.

The dynamic stability under the representative electric fields along the *out-of-plane* is confirmed by the phonon dispersions of the BAAs/MoSSe-I and BAAs/MoSSe-II, as shown in Fig. 1. Interestingly, the ZA phonon branch exhibits an almost flat phonon band, primarily due to the significant mass difference between the B and As, Mo atoms, which widely exists in boron-based compounds $h\text{-BX}$ ($X = \text{N, P, As, and Sb}$), as previously reported in literature [52,61]. Meanwhile, as illustrated by the magnified low-frequency phonon spectrum (Supplemental Material, Fig. S2 [60]), phonon softening happens at the electric field strength of 0.2 V \AA^{-1} , while phonon hardening occurs for the reversed electric field for BAAs/MoSSe-I. This phenomenon of phonon softening

or hardening in BAAs/MoSSe-II is not as pronounced as in BAAs/MoSSe-I, which demonstrates the subtle modification of the phonon spectra by the external electric field. Additionally, the thermodynamic stability of BAAs/MoSSe-I and BAAs/MoSSe-II is also verified by the Ab-Initio Molecular Dynamics (AIMD) simulations at 500 K as shown in Supplemental Material, Fig. S3 [60]. When considering the LO-TO splitting, only the high-frequency optical phonon branches change slightly, as shown in Supplemental Material, Fig. S4 [60]. Some changes can be found near the center of the Brillouin zone for the low-frequency optical phonon branches under the electric fields. Besides, the changes with the electric field can also be verified by the partial density of states ($pDOS$), as depicted in Fig. 1. For BAAs/MoSSe-I, the peak strength of the S atoms decreases with the increasing of the electric fields from -0.2 to $+0.2 \text{ V \AA}^{-1}$, while for the BAAs/MoSSe-II, the $pDOS$ of S and Se atoms without electric field stays higher than that under the electric field strength of $\pm 0.2 \text{ V \AA}^{-1}$. The higher phonon density of state means more phonon aggregation and smoother phonon branches,

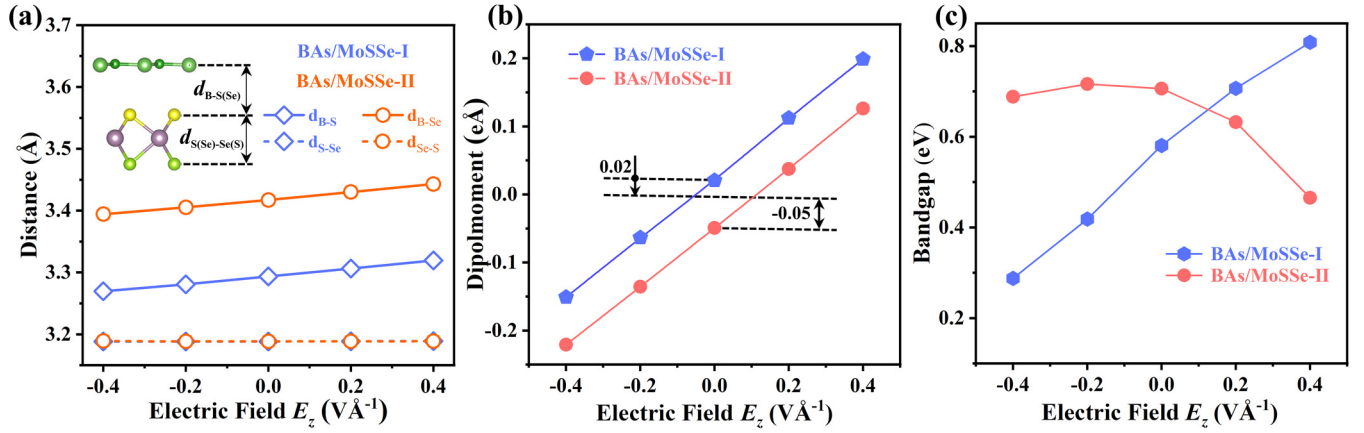


FIG. 2. The (a) distance of B and Se (S) atoms to S(Se) atoms, (b) dipole moment, and (c) band gap as a function of representative electric fields for BAs/MoSSe-I and BAs/MoSSe-II.

which eventually leads to lower phonon group velocities and lower thermal conductivity. The above analysis of the p DOS is in good agreement with the change of thermal conductivity under external electric field.

The in-plane lattice constants of both BAs/MoSSe-I and BAs/MoSSe-II are 3.31 Å, and the interlayer distance for B-S (B-Se) and S-Se (Se-S) planes are 3.29 (3.41) and 3.18 (3.18) Å, respectively. Compared with the hardly changed distance of S and Se atoms' plane, the variation of interlayer distance for B-S (BAs/MoSSe-I) and B-Se (BAs/MoSSe-II) is considerable, which is mainly attributed to the electronegativity difference between S (2.58) and Se (2.55) atoms. With the increasing electric field strength, the interlayer distance between BAs and S(Se) atoms' plane ($d_{B-S(Se)}$) is modified more obviously than that of S and Se atoms plane (d_{S-Se}) as shown in Fig. 2(a). Additionally, the asymmetry of MoSSe induced the charge center to deviate from the BAs plane with the positive electric field applied, resulting in the enlarged interlayer distance. On the contrary, the interlayer distance is shortened with the negative electric field applied. Besides, the dipole moment increases monotonically with the increasing electric fields for both BAs/MoSSe-I and BAs/MoSSe-II, and the direction is overturned with the revised external electric field applied as shown in Fig. 2(b). As a vector, the result of the dipole moment is calculated by the following formula:

$$\vec{p} = q * \vec{d}, \quad (1)$$

where the \vec{p} is the dipole moment vector, q is the magnitude of the charge distribution, and \vec{d} is the vector pointing from the negative to the positive charge. In conjunction with the charge distribution and direction of vector, the changes for interlayer distance and dipole moment exhibit a monotonic trend with the variation of the electric field, which is in good agreement with previous studies [33,35]. It is worth noting that a slight difference in dipole moment can be found (depicted by the dashed-dotted line) between the twins' heterostructures without electric field, which is mainly attributed to the electronegativity difference between S and Se atoms and the different arrangements of BAs and MoSSe.

Benefiting from the different arrangements of BAs/MoSSe-I and BAs/MoSSe-II, the band gap can

be modulated effectively by external electric field as demonstrated in Fig. 2(c). In detail, the gradient difference between the conduction-band minimum (CBM) and valence-band maximum (VBM) consistently increases with the growing electric field strength in BAs/MoSSe-I, which locate at the high-symmetry K point, maintaining a direct band gap all the time, as shown in Supplemental Material, Fig. S5 and Fig. S6 [60]. In the case of BAs/MoSSe-II, this upward trend is only sustained within the range of -0.4 to 0 V Å⁻¹. As the electric field strength further increases, the gradient difference diminishes, and a shift of the VBM from the K point to the Γ point occurs, as depicted in Supplemental Material, Fig. S7 [60].

To further explore the underlying physical mechanisms of the different changes of the band gap for the two configurations, the density of states (DOS) of each element as well as the atomic orbital projected density of states (p DOS) are presented in Supplemental Material, Fig. S8 [60] and Fig. 3. Notably, the influencers of the VBM and CBM are mainly focused on the As and Mo elements. Detailed analysis shows that the d_z^2 orbital of the Mo element noticeably shifts upward with increasing electric field strength in BAs/MoSSe-I, ultimately leading to a continuous enlargement of the band gap [Fig. 3(a)]. For BAs/MoSSe-II, the p_z orbital of As atom dominates the VBM under the range of -0.4 to 0 V Å⁻¹ [Fig. 3(d)]. However, with the sustained enhancement of the electric field, the d_z^2 orbital of the Mo element gradually shifts upward. Eventually, the VBM transitions from the p_z orbital of the As element to the d_z^2 orbital of the Mo element. Simultaneously, the VBM also transforms from K to Γ point, completing the direct to indirect band-gap conversion [Fig. 3(c)]. This variation's trend with the external electric field as well as the transition between direct and indirect band gap has also been well validated in previous studies [62–65]. While it is known that the PBE functional tends to underestimate the band gaps, this does not affect the research of the regulation trend of the band gap by the electric field. Here, we mainly focus on the regulation of thermal conductivity by the electric field of the different stacking configurations of BAs/MoSSe-I and BAs/MoSSe-II. Undoubtedly, the broad regulatory capabilities of the twins' heterostructures (BAs/MoSSe-I and BAs/MoSSe-II) bring

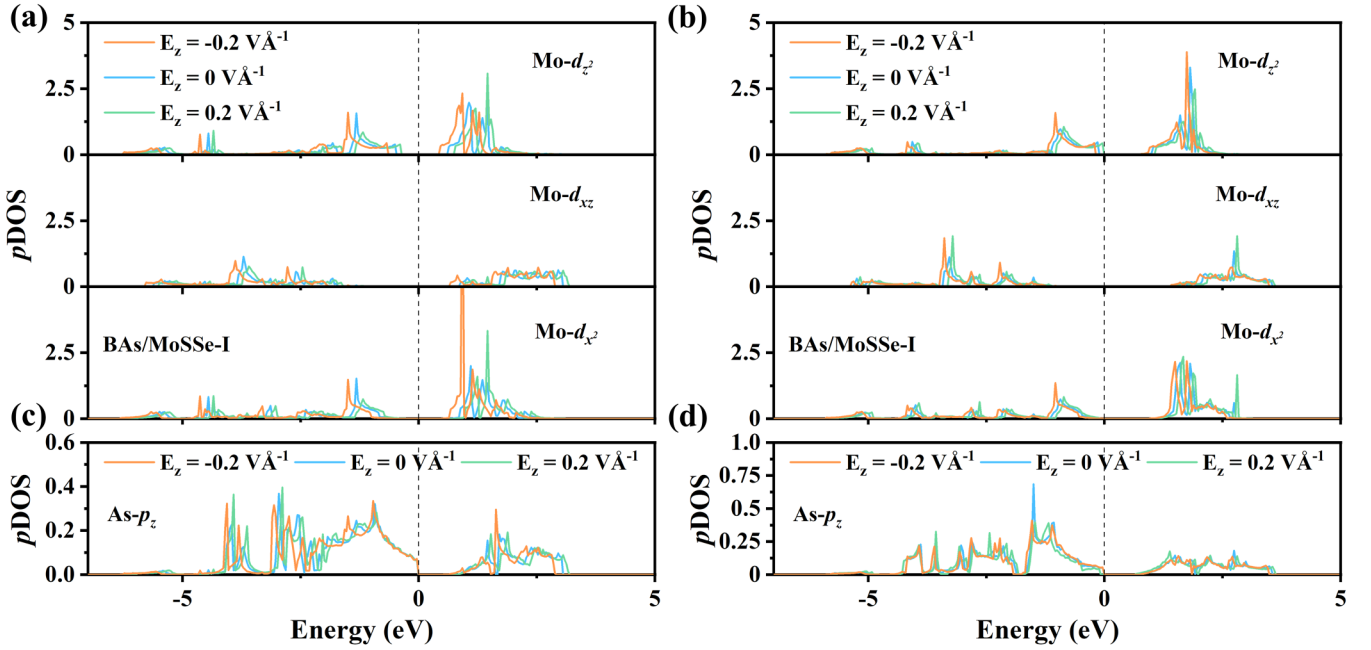


FIG. 3. The major p DOS of As and Mo atoms under the external electric field of -0.2 , 0 , and 0.2 V \AA^{-1} for (a), (c) BAS/MoSSe-I and (b), (d) BAS/MoSSe-II.

wide range and multidomain applications such as optoelectronic devices, solar cells, energy storage field, etc. [66,67].

As shown in Fig. 4(a), the evolution of the background's edges illustrates the relationship between the thermal conductivity of twin heterostructures and their dependence on the external electric field, which is much like half of a Tai chi pattern. In detail, the thermal conductivity of BAS/MoSSe-I is $14.70 \text{ W m}^{-1} \text{ K}^{-1}$ without electric field, which is slightly higher than that of BAS/MoSSe-II ($11.48 \text{ W m}^{-1} \text{ K}^{-1}$). The slight difference between the twins' heterostructures can be attributed to the different stacking arrangements. The convergence test of cutoff radius and Q grid for the twin heterostructures are carried out to ensure the accuracy of the calculations of thermal conductivity, as shown in Supplemental Material, Fig. S9 and Supplemental Material, Fig. S10 [60]. Based on convergence test results, the sixth-nearest neighbor cutoff radius as well as the $101 \times 101 \times 1 Q$ grids are set along with the following calculations under electric fields. Interestingly, the thermal conductivity of BAS/MoSSe-II is almost 22.4 times that of BAS/MoSSe-I when $E_z = -0.2 \text{ V \AA}^{-1}$. Further analysis suggests that the huge differential response comes from the large low-frequency phonons' contribution to thermal conductivity, which mainly focus on the range of $2 \sim 4 \text{ THz}$ as shown in Fig. 4(b). Additionally, under the electronic field strength of -0.2 V \AA^{-1} , the thermal conductivity of optical phonon branches is largely inhibited for BAS/MoSSe-I, while greatly enhanced for BAS/MoSSe-II [Fig. 4(c)]. This optical-branch dependent thermal conductivity comparing with the low acoustic phonon branch contribution is consistent with the variation of the phonon dispersion under the external electric fields. Meanwhile, the variation of the thermal conductivity and different phonon branches under the external electric field with respect to temperature is confirmed in Fig. 4(d) and Supple-

mental Material, Fig. S11 [60], respectively. Obviously, the percentage contribution of optical phonon branches is much lower than 50% for BAS/MoSSe-II at -0.2 V \AA^{-1} (Supplemental Material, Fig. S11(e) [60]). Consequently, the low thermal conductivity together with the low percentage contribution of optical phonon branches finally lead to the low thermal conductivity of BAS/MoSSe-I at the electronic field of -0.2 V \AA^{-1} .

The phonon mean-free path (MFP) is employed to evaluate the influence of phonon characteristic length on total thermal conductivity, which is of great significance to the thermal management system design based on nanostructures. Considering the high contribution of the optical phonon branches as well as the steep change trend of the thermal conductivity at about $2 \sim 4 \text{ THz}$, the optical phonon branches dominate the MFP undoubtedly, which is also examined by the 50% cumulated thermal conductivity in Fig. 4(e). The corresponding MFP is about 15 nm at the -0.2 V \AA^{-1} for BAS/MoSSe-I, which is considerably smaller than that of the BAS/MoSSe-II (100 nm) measured by the 50% cumulated thermal conductivity. To further understand the size effect on the thermal conductivity, the cumulated thermal conductivity *vs* characteristic length scales of the materials is investigated in Fig. 4(f). Herein, boundary scattering is included from the finite size with the consideration of a totally diffusive scattering at the boundary [$p = 0$ in Eq. (2)]. The thermal conductivity converges to the constant with the limited size up to the 10^6 nm under the different electric fields, and the larger of MFP, the easier to design the finite-size thermal conductivity, which is useful to tailor the thermal conductivity for the thermoelectrics and thermal management by nanostructure engineering.

To further understand the differential thermal conductivity under external electric field of the BAS/MoSSe twins'

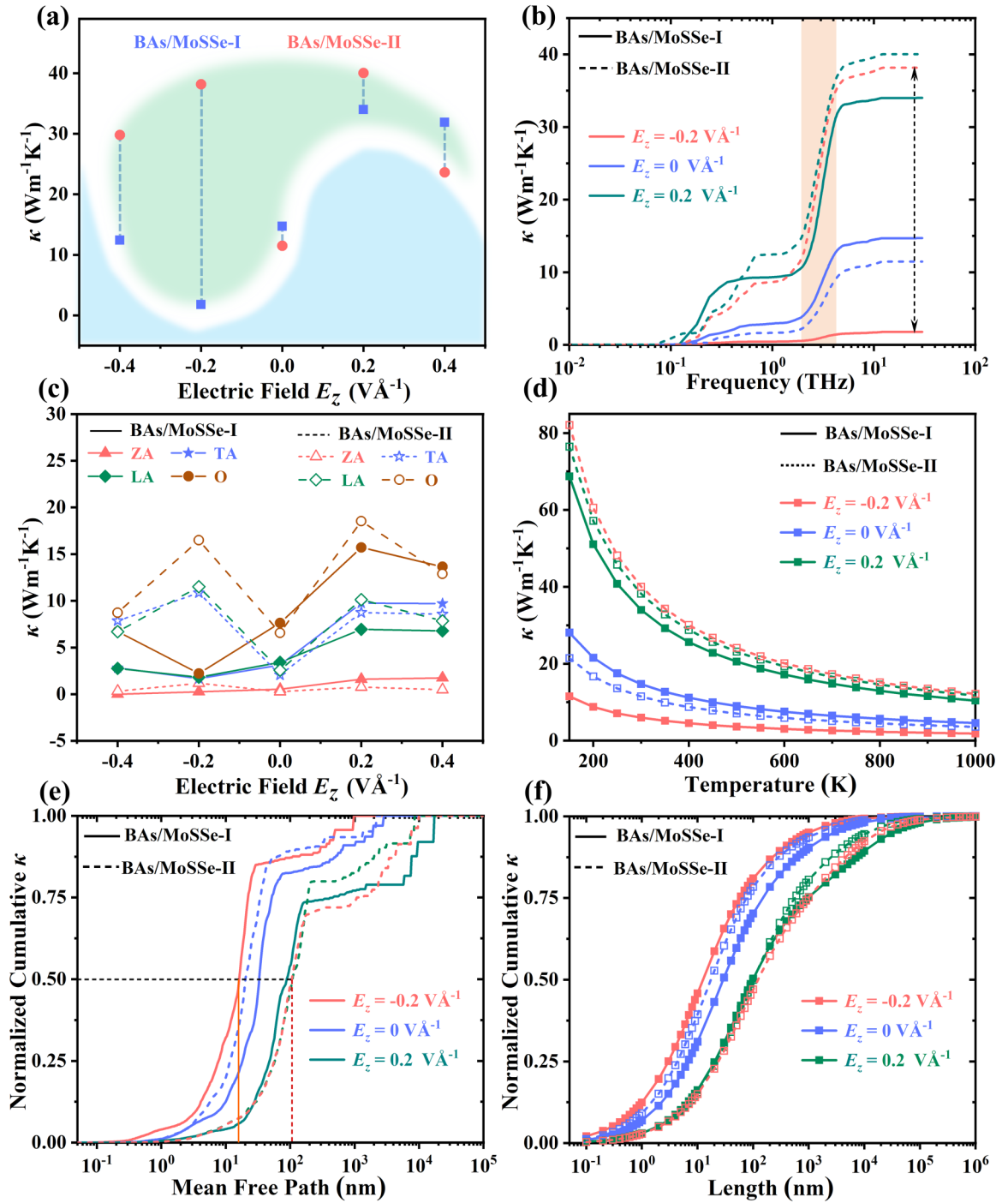


FIG. 4. The comparison between BA/MoSSe-I and BA/MoSSe-II of (a) thermal conductivity under representative electric fields, (b) frequency-dependent cumulative thermal conductivity at 300 K with ($\pm 0.2 \text{ V}\text{\AA}^{-1}$) and without electric field, (c) the thermal conductivity contribution of different phonon branches as a function of electric fields, (d) the temperature-dependent thermal conductivity with ($\pm 0.2 \text{ V}\text{\AA}^{-1}$) and without electric field, (e) normalized cumulative thermal conductivity with respect to the mean-free path (MFP), and (f) the size-dependent thermal conductivity considering boundary scattering.

heterostructure, the lattice thermal conductivity of BA/MoSSe-I and BA/MoSSe-II is refined, analyzed by phonon modes according to the phonon Boltzmann transport equation as shown in Fig. 5 and Supplemental Material, Fig. S12 [60]. A large reduction of the phonon relaxation time can be found under the $-0.2 \text{ V}\text{\AA}^{-1}$ compared with the primary state of BA/MoSSe-I, which is consistent with the change

of the lower thermal conductivity. Meanwhile, the huge enhancement of the phonon relaxation time corresponds to the enlarged thermal conductivity at $0.2 \text{ V}\text{\AA}^{-1}$. This result is different from that of BA/MoSSe-II, of which the enhanced phonon relaxation time can be found both at 0.2 and $-0.2 \text{ V}\text{\AA}^{-1}$ electric fields. Meanwhile, the variation of group velocity and phase space under electric field is

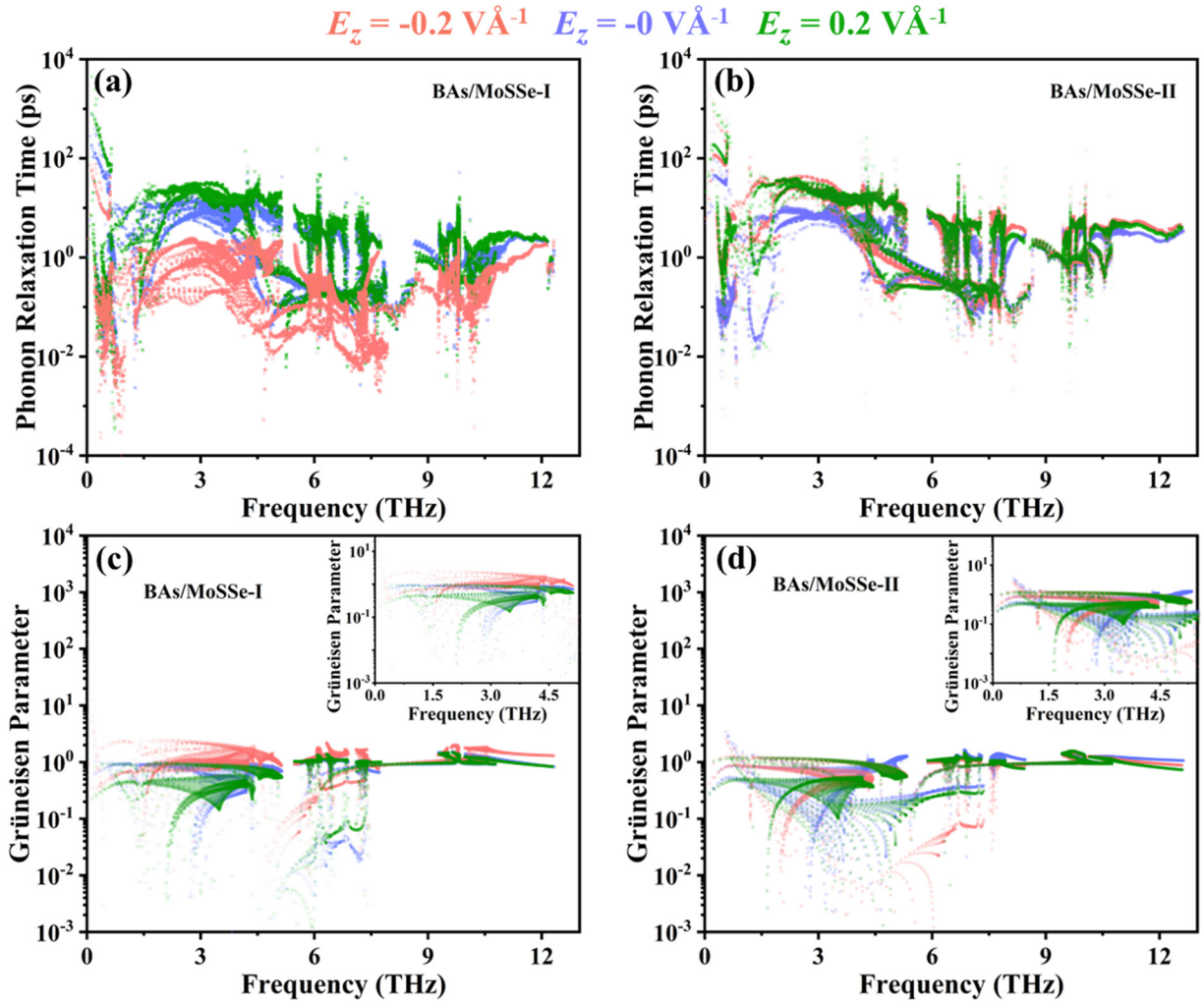


FIG. 5. Comparison of mode-level analysis of BAs/MoSSe-I and BAs/MoSSe-II under representative electric fields as a function of frequency for (a), (b) phonon relaxation time and (c), (d) Grüneisen parameter, respectively.

demonstrated in Supplemental Material, Fig. 12 [60]. And, the minor changes of phonon group velocity are verified in Supplemental Material, Fig. S12 [60], which is consistent with previous discussions based on the p DOS as shown in Fig. 1. Specifically, the statistical data of the total volume of phase under -0.2 , 0 , and 0.2 V \AA^{-1} electric fields are 4.066 , 4.048 , and 4.069×10^{-3} for BAs/MoSSe-I, and 3.880 , 3.867 , and 3.868×10^{-3} for BAs/MoSSe-II, respectively. Thus, the slight variations in phonon group velocity and phase space further reinforce the predominant influence of electric field regulation on phonon relaxation time and anharmonicity, which ultimately affects thermal conductivity. Subsequently, the Grüneisen parameter of BAs/MoSSe-I and BAs/MoSSe-II as shown in Figs. 5(c) and 5(d) is studied to understand the anharmonicity of phonons. As a result, strong phonon anharmonicity especially for the low-frequency regions is induced by applying -0.2 V \AA^{-1} electric field, resulting in the lower phonon relaxation time comparing with the original one as well as that of 0.2 V \AA^{-1} electric field for BAs/MoSSe-I. At the same times, the Grüneisen parameter of the BAs/MoSSe-II reveals the weakening effect for $\pm 0.2 \text{ V \AA}^{-1}$ electric fields, indicating the enlarged phonon

relaxation time, which finally leads to the enhanced thermal conductivity. Under the above analysis, the strong phonon anharmonicity (Grüneisen parameter) induced by the external electric field may be responsible for the changes of the thermal conductivity of the twins' heterostructures compared with the weakened phonon harmonicity evaluated by the group velocity.

The differences of charge density under $\pm 0.2 \text{ V \AA}^{-1}$ electric fields are carried out to probe the in-depth regulation mechanism of electrons as shown in Fig. 6. The result shows that the difference between BAs/MoSSe-I and BAs/MoSSe-II twins' heterostructures under -0.2 V \AA^{-1} electric field [Figs. 6(a) and 6(d)] is larger than that in 0.2 V \AA^{-1} electric field [Figs. 6(b) and 6(e)] marked by the orange and blue ellipses dashed-dotted line, respectively, which is also confirmed by the plane average differential charge density [Figs. 6(c) and 6(f)]. Furthermore, the quantized charge transfer of B and As atoms is shown in Figs. 6(g) and 6(h); the result indicates that charge transfer occurs not only between in-plane atoms but also layers. With the increasing electric field, the charge transfer from BAs layer to MoSSe layer progressively shrinks for BAs/MoSSe-I, while it increases

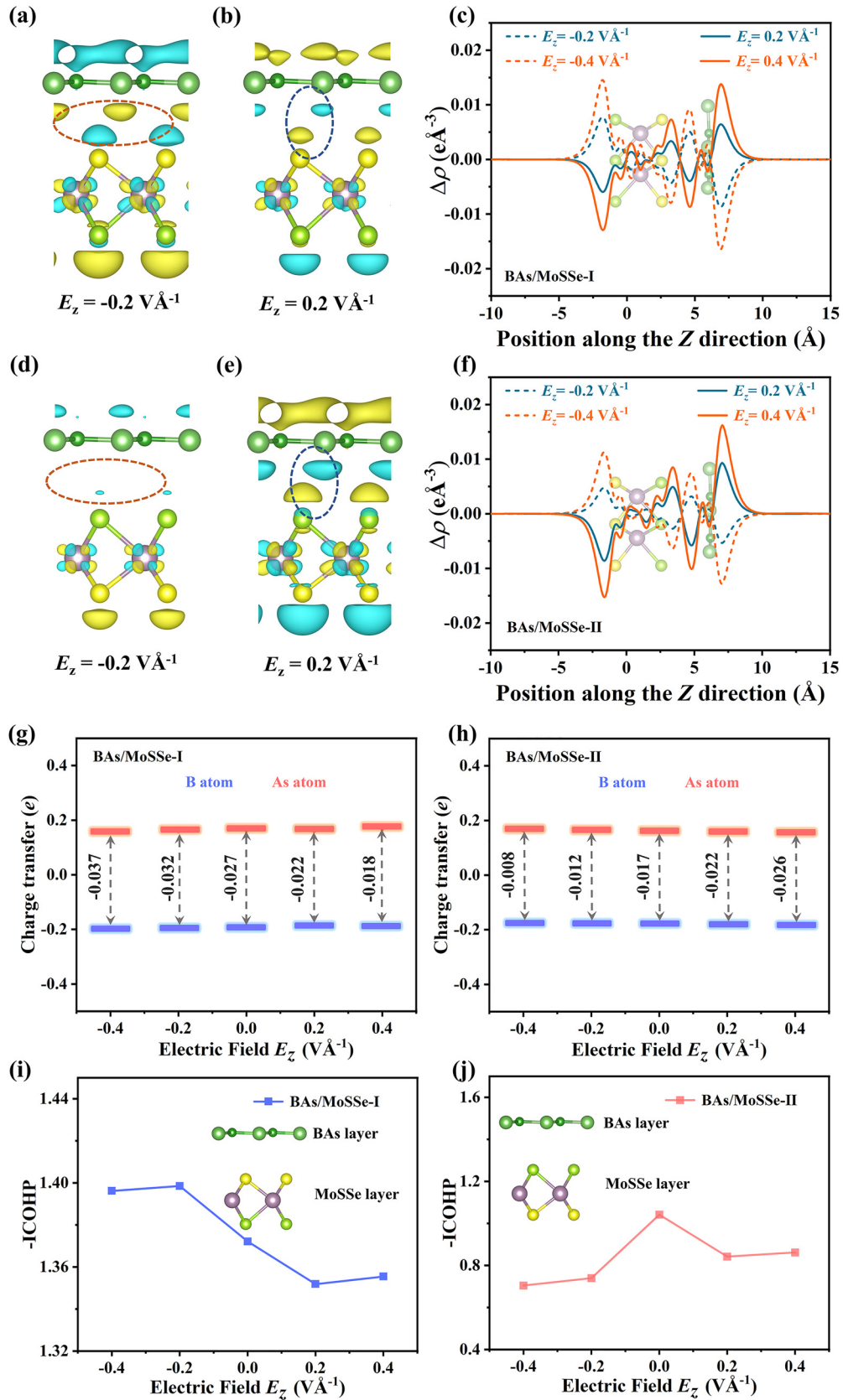


FIG. 6. The difference in charge density under representative electric fields at $\pm 0.2 \text{ V\AA}^{-1}$ [$\Delta\rho = \rho(E_z) - \rho(E_z = 0)$] and the average of the plane differential charge density along the out-of-plane direction at $\pm 0.2, \pm 0.4 \text{ V\AA}^{-1}$ of (a)–(c) BAs/MoSSe-I, and (d)–(f) BAs/MoSSe-II. The isosurface is set as 1.2×10^{-4} , while yellow and blue refer to positive accumulation and negative depletion of charge, respectively. The charge transfer (g), (h) and $-\text{ICOHP}$ (i), (j) as a function of electric field of BAs/MoSSe-I and BAs/MoSSe-II, while the value represents cumulative charge transfer of B and As atoms.

for BAs/MoSSe-II. This monotonic change of charge-transfer trend for the twins' heterostructures is consistent with that of the dipole moment, as shown in Fig. 2(b). The trend difference is the direction in which the electric field is applied by the two configurations. It is worth noting that the trend of charge transfer between B atoms and As atoms with the change of electric field is not entirely monotonically increasing in BAs/MoSSe-I, as shown in Supplemental Material, Fig. S13 [60]. This implies that the change of the thermal conductivity under the electric field may cause local disturbance, as demonstrated in Fig. 4(a), showing a slight decrease of the thermal conductivity under 0.4 V \AA^{-1} comparing with 0.2 V \AA^{-1} . Nevertheless, this does not affect the overall regulatory trend of the electric field on thermal conductivity and band structure.

In addition, the integrated crystal orbital Hamiltonian populations (ICOHP) are employed to further explore the impact of interlayer charge transfer on interlayer interactions, as shown in Figs. 6(i) and 6(j). It is known that positive ICOHP values represent antibonding states, while negative values represent bonding states between atoms. Here, we numerically solved the interactions between B, As atoms of BAs layer and Mo, S, Se atoms of the MoSSe layer systematically. The results indicate that for the BAs/MoSSe-I, with the reduction of interlayer charge transfer, the value of $-\text{ICOHP}$ gradually decreases, implying a weakening of interlayer interactions, while for the BAs/MoSSe-II, an increase of charge transfer leads to a decrease of $-\text{ICOHP}$ when the external electric field is greater than 0 V \AA^{-1} . Further investigations reveal that the interaction between As and Mo atoms finally dominates the result of the $-\text{ICOHP}$. This result is consistent with the outcomes of band-gap modulation by the electric field at $0.2 - 0.4 \text{ V \AA}^{-1}$, which is mainly attributed to the changes in the charge-density distribution of Mo atoms. In short, for BAs/MoSSe-I, under negative electric field, as the electric field strength increases, strengthening of interlayer interactions induced by charge transfer enhances phonon anharmonicity, leading to a decrease in the thermal conductivity. Conversely, under positive electric field, as the electric field strength increases, weakening of interlayer interactions induced by charge transfer diminishes phonon anharmonicity and results in an increase in the thermal conductivity. For BAs/MoSSe-II, regardless of whether under a positive or negative electric field, the increase in electric field strength weakens interlayer interactions by charge transfer, reducing phonon anharmonicity, and ultimately resulting in an increase in the thermal conductivity. The decrease in phonon anharmonicity with weakened interlayer interactions is consistent with previous reports [68,69], further validating our findings and analysis.

As is widely recognized, reducing the intrinsic lattice thermal conductivity is of paramount importance for enhancing thermoelectric performance of materials, while increasing the thermal conductivity facilitates internal heat dissipation within the material. Under identical conditions, a reduction in lattice thermal conductivity significantly enhances the thermoelectric performance of materials, which holds substantial practical value for thermoelectric energy conversion. Our

investigation indicates that with the application of an electric field, especially in a certain direction, there is a significant decrease in the thermal conductivity, thus offering a highly effective strategy for enhancing the thermoelectric performance of materials, despite the possible influence of various factors. Additionally, under certain electric field conditions, there is a notable increase in the thermal conductivity, which greatly facilitates internal heat diffusion within the material. This provides valuable solutions and strategies for efficient thermal management in diverse applications, such as electric devices and electric vehicles. Most importantly, by constructing different heterostructures, we can nondestructively and efficiently regulate the thermal conductivity by varying electric fields, thereby facilitating its crucial applications in both thermoelectric energy conversion and device thermal managements. Furthermore, we can also design electrically controlled thermal devices based on the series-parallel topology of such heterostructures, enabling the control of heat-flow channels.

IV. CONCLUSION

In summary, we comprehensively investigated the external electric field modulating thermal transport properties of the BAs/MoSSe twins' heterostructures originating from monolayer BAs and MoSSe based on the state-of-the-art DFT calculations. The different responses of the thermal conductivity can be clearly noticed under the electric fields ranging from -0.4 to 0.4 V \AA^{-1} . Remarkably, the thermal conductivity of BAs/MoSSe-II is almost 22.4 times that of BAs/MoSSe-I under -0.2 V \AA^{-1} electric field. Detailed analysis demonstrates that the interlayer charge-density redistribution under electric fields leads to the weakening (or strengthening) interatomic interaction, making the corresponding enhanced (or weakened) phonon anharmonicity, which finally results in reduced (or increased) thermal conductivity. The electric field modulated thermal conductivity of BAs/MoSSe vdW twin heterostructures shown in this work is remarkable for its value of physical and engineering applications in thermoelectrics and thermal management, etc.

ACKNOWLEDGMENTS

This work is supported by the National Natural Science Foundation of China (Grants No. 52006057, No. 51906097, No. 11904324, and No. 12274374), the Fundamental Research Funds for the Central Universities (Grants No. 531119200237 and No. 541109010001), the State Key Laboratory of Advanced Design and Manufacturing for Vehicle Body at Hunan University (Grant No. 52175013), and the Natural Science Foundation of Henan Province of China (Grant No. 222300420551). This work is also supported by the National Key R&D Program of China (Grant No. 2023YFB2408100) and Natural Science Foundation of Chongqing, China (Grant No. CSTB2022NSCQ-MSX0332). The numerical calculations have been done on the supercomputing system of the E.T. Cluster.

- [1] K. S. Novoselov, A. Mishchenko, A. Carvalho, and A. H. Castro Neto, 2D materials and van der Waals heterostructures, *Science* **353**, 9439 (2016).
- [2] J. Shim, H.-Y. Park, D.-H. Kang, J.-O. Kim, S.-H. Jo, Y. Park, and J.-H. Park, Electronic and optoelectronic devices based on two-dimensional materials: From fabrication to application, *Adv. Electron. Mater.* **3**, 1600364 (2017).
- [3] N. R. Pradhan, S. Talapatra, M. Terrones, P. M. Ajayan, and L. Balicas, Optoelectronic properties of heterostructures: The most recent developments based on graphene and transition-metal dichalcogenides, *IEEE Nanotechnol. Mag.* **11**, 18 (2017).
- [4] J. F. Sierra, J. Fabian, R. K. Kawakami, S. Roche, and S. O. Valenzuela, van der Waals heterostructures for spintronics and opto-spintronics, *Nat. Nanotechnol.* **16**, 8 (2021).
- [5] P. V. Pham, S. C. Bodepudi, K. Shehzad, Y. Liu, Y. Xu, B. Yu, and X. Duan, 2d heterostructures for ubiquitous electronics and optoelectronics: Principles, opportunities, and challenges, *Chem. Rev.* **122**, 6514 (2022).
- [6] J. Su, G.-D. Li, X.-H. Li, and J.-S. Chen, 2D/2D Heterojunctions for catalysis, *Adv. Sci.* **6**, 1801702 (2019).
- [7] X. Zheng, S. S. Mofarah, C. Cazorla, R. Daiyan, A. A. Esmailpour, J. Scott, Y. Yao, S. Lim, V. Wong, E. Y. Chen, H. Arandiyani, P. Koshy, and C. C. Sorrell, Decoupling the impacts of engineering defects and band gap alignment mechanism on the catalytic performance of holey 2D CeO_{2-x} -based heterojunctions, *Adv. Funct. Mater.* **31**, 2103171 (2021).
- [8] S. Mitra, S. Kakkar, T. Ahmed, and A. Ghosh, Graphene- WS_2 van der Waals hybrid heterostructure for photodetector and memory device applications, *Phys. Rev. Appl.* **14**, 064029 (2020).
- [9] L. Ye, H. Li, Z. Chen, and J. Xu, Near-infrared photodetector based on MoS_2 /Black Phosphorus heterojunction, *ACS Photonics* **3**, 692 (2016).
- [10] L. Britnell, R. V. Gorbachev, R. Jalil, B. D. Belle, F. Schedin, A. Mishchenko, T. Georgiou, M. I. Katsnelson, L. Eaves, S. V. Morozov, N. M. R. Peres, J. Leist, A. K. Geim, K. S. Novoselov, and L. A. Ponomarenko, Field-effect tunneling transistor based on vertical graphene heterostructures, *Science* **335**, 947 (2012).
- [11] Y.-C. Lin, R. K. Ghosh, R. Addou, N. Lu, S. M. Eichfeld, H. Zhu, M.-Y. Li, X. Peng, M. J. Kim, L.-J. Li, R. M. Wallace, S. Datta, and J. A. Robinson, Atomically thin resonant tunnel diodes built from synthetic van der Waals heterostructures, *Nat. Commun.* **6**, 7311 (2015).
- [12] M. Sup Choi, G.-H. Lee, Y.-J. Yu, D.-Y. Lee, S. Hwan Lee, P. Kim, J. Hone, and W. Jong Yoo, Controlled charge trapping by molybdenum disulphide and graphene in ultrathin heterostructured memory devices, *Nat. Commun.* **4**, 1624 (2013).
- [13] L. Yin, R. Cheng, Y. Wen, C. Liu, and J. He, Emerging 2d memory devices for in-memory computing, *Adv. Mater.* **33**, 2007081 (2021).
- [14] T. Li, J. Yu, G. Nie, B.-P. Zhang, and Q. Sun, The ultralow thermal conductivity and ultrahigh thermoelectric performance of fluorinated Sn_2Bi sheet in room temperature, *Nano Energy* **67**, 104283 (2020).
- [15] C. Wan, Y. Wang, N. Wang, W. Norimatsu, M. Kusunoki, and K. Koumoto, Development of novel thermoelectric materials by reduction of lattice thermal conductivity, *Sci. Technol. Adv. Mater.* **11**, 044306 (2010).
- [16] X. Meng, T. Pandey, J. Jeong, S. Fu, J. Yang, K. Chen, A. Singh, F. He, X. Xu, J. Zhou, W.-P. Hsieh, A. K. Singh, J.-F. Lin, and Y. Wang, Thermal conductivity enhancement in MoS_2 under extreme strain, *Phys. Rev. Lett.* **122**, 155901 (2019).
- [17] H. Xie, T. Ouyang, É. Germaneau, G. Qin, M. Hu, and H. Bao, Large tunability of lattice thermal conductivity of monolayer silicene via mechanical strain, *Phys. Rev. B* **93**, 075404 (2016).
- [18] Y. Kuang, L. Lindsay, and B. Huang, Unusual enhancement in intrinsic thermal conductivity of multilayer graphene by tensile strains, *Nano Lett.* **15**, 6121 (2015).
- [19] K. F. Murphy, B. Piccione, M. B. Zanjani, J. R. Lukes, and D. S. Gianola, Strain- and defect-mediated thermal conductivity in silicon nanowires, *Nano Lett.* **14**, 3785 (2014).
- [20] D.-S. Tang, G.-Z. Qin, M. Hu, and B.-Y. Cao, Thermal transport properties of GaN with biaxial strain and electron-phonon coupling, *J. Appl. Phys.* **127**, 035102 (2020).
- [21] J. Song, Z. Xu, X. He, C. Cai, Y. Bai, L. Miao, and R. Wang, Effect of strain and defects on the thermal conductance of the graphene/hexagonal boron nitride interface, *Phys. Chem. Chem. Phys.* **22**, 11537 (2020).
- [22] S. Bazrafshan and A. Rajabpour, Engineering of thermal transport in graphene using grain size, strain, nitrogen and boron doping; a multiscale modeling, *Int. J. Heat Mass Transf.* **123**, 534 (2018).
- [23] M. Ohnishi and J. Shiomi, Strain-induced band modulation of thermal phonons in carbon nanotubes, *Phys. Rev. B* **104**, 014306 (2021).
- [24] S. Jiang, J. Shan, and K. F. Mak, Electric-field switching of two-dimensional van der Waals magnets, *Nat. Mater.* **17**, 406 (2018).
- [25] C. Xu, P. Chen, H. Tan, Y. Yang, H. Xiang, and L. Bellaiche, Electric-field switching of magnetic topological charge in type-I multiferroics, *Phys. Rev. Lett.* **125**, 037203 (2020).
- [26] Q. Wu, L. Cao, Y. S. Ang, and L. K. Ang, Semiconductor-to-metal transition in bilayer MoSi_2N_4 and WSi_2N_4 with strain and electric field, *Appl. Phys. Lett.* **118**, 113102 (2021).
- [27] Y. Han, C. Nickle, Z. Zhang, H. P. A. G. Astier, T. J. Duffin, D. Qi, Z. Wang, E. del Barco, D. Thompson, and C. A. Nijhuis, Electric-field-driven dual-functional molecular switches in tunnel junctions, *Nat. Mater.* **19**, 843 (2020).
- [28] J. L. Collins, A. Tadich, W. Wu, L. C. Gomes, J. N. B. Rodrigues, C. Liu, J. Hellerstedt, H. Ryu, S. Tang, S.-K. Mo, S. Adam, S. A. Yang, M. S. Fuhrer, and M. T. Edmonds, Electric-field-tuned topological phase transition in ultrathin Na_3Bi , *Nature (London)* **564**, 7736 (2018).
- [29] Z. Hao, A. M. Zimmerman, P. Ledwith, E. Khalaf, D. H. Najafabadi, K. Watanabe, T. Taniguchi, A. Vishwanath, and P. Kim, Electric field-tunable superconductivity in alternating-twist magic-angle trilayer graphene, *Science* **371**, 1133 (2021).
- [30] F. Zhang, H. Zhang, S. Krylyuk, C. A. Milligan, Y. Zhu, D. Y. Zemlyanov, L. A. Bendersky, B. P. Burton, A. V. Davydov, and J. Appenzeller, Electric-field induced structural transition in vertical MoTe_2 - and $\text{Mo}_{1-x}\text{W}_x\text{Te}_2$ -based resistive memories, *Nat. Mater.* **18**, 55 (2019).
- [31] P. Wang, Y. Zong, H. Liu, H. Wen, Y. Liu, H.-B. Wu, and J.-B. Xia, Vertical strain and electric field tunable band alignment in Type-II ZnO/MoSSe van der Waals heterostructures, *Phys. Chem. Chem. Phys.* **23**, 1510 (2021).
- [32] J. F. Ihlefeld, B. M. Foley, D. A. Scrymgeour, J. R. Michael, B. B. McKenzie, D. L. Medlin, M. Wallace, S. Trolier-McKinstry, and P. E. Hopkins, Room-temperature voltage tunable phonon thermal conductivity via reconfigurable interfaces in ferroelectric thin films, *Nano Lett.* **15**, 1791 (2015).

- [33] G. Qin, Z. Qin, S.-Y. Yue, Q.-B. Yan, and M. Hu, External electric field driving the ultra-low thermal conductivity of silicene, *Nanoscale* **9**, 7227 (2017).
- [34] Z. Chang, K. Yuan, Z. Sun, X. Zhang, Y. Gao, G. Qin, and D. Tang, Ultralow lattice thermal conductivity and dramatically enhanced thermoelectric properties of monolayer InSe Induced by an external electric field, *Phys. Chem. Chem. Phys.* **23**, 13633 (2021).
- [35] Z. Yang, K. Yuan, J. Meng, and M. Hu, Electric field tuned anisotropic to isotropic thermal transport transition in monolayer borophene without altering its atomic structure, *Nanoscale* **12**, 19178 (2020).
- [36] Y. Quan, S.-Y. Yue, and B. Liao, Electric field effect on the thermal conductivity of wurtzite GaN, *Appl. Phys. Lett.* **118**, 162110 (2021).
- [37] E. Zhou, D. Wei, J. Wu, G. Qin, and M. Hu, Electrically-driven robust tuning of lattice thermal conductivity, *Phys. Chem. Chem. Phys.* **24**, 17479 (2022).
- [38] S. Deng, J. Yuan, Y. Lin, X. Yu, D. Ma, Y. Huang, R. Ji, G. Zhang, and N. Yang, Electric-field-induced modulation of thermal conductivity in poly(vinylidene fluoride), *Nano Energy* **82**, 105749 (2021).
- [39] W. Shi and Z. Wang, Mechanical and electronic properties of Janus monolayer transition metal dichalcogenides, *J. Phys.: Condens. Matter* **30**, 215301 (2018).
- [40] D. D. Vo, T. V. Vu, S. Al-Qaisi, H. D. Tong, T. S. Le, C. V. Nguyen, H. V. Phuc, H. L. Luong, H. R. Jappor, M. M. Obeid, and N. N. Hieu, Janus monolayer PtSSe under external electric field and strain: A first principles study on electronic structure and optical properties, *Superlatt. Microstruct.* **147**, 106683 (2020).
- [41] L. Dong, J. Lou, and V. B. Shenoy, Large in-plane and vertical piezoelectricity in Janus transition metal dichalcogenides, *ACS Nano* **11**, 8242 (2017).
- [42] M. Yagmurcukardes, C. Sevik, and F. M. Peeters, Electronic, vibrational, elastic, and piezoelectric properties of monolayer Janus MoSTe phases: A first-principles study, *Phys. Rev. B* **100**, 045415 (2019).
- [43] Y. Guo, S. Zhou, Y. Bai, and J. Zhao, Enhanced piezoelectric effect in Janus group-III chalcogenide monolayers, *Appl. Phys. Lett.* **110**, 163102 (2017).
- [44] C. Zhang, Y. Nie, S. Sanvito, and A. Du, First-principles prediction of a room-temperature ferromagnetic Janus VSSe monolayer with piezoelectricity, ferroelasticity, and large valley polarization, *Nano Lett.* **19**, 1366 (2019).
- [45] Y. C. Cheng, Z. Y. Zhu, M. Tahir, and U. Schwingenschlögl, Spin-orbit-induced spin splittings in polar transition metal dichalcogenide monolayers, *Europhys. Lett.* **102**, 57001 (2013).
- [46] T. Hu, F. Jia, G. Zhao, J. Wu, A. Stroppa, and W. Ren, Intrinsic and anisotropic Rashba spin splitting in Janus transition-metal dichalcogenide monolayers, *Phys. Rev. B* **97**, 235404 (2018).
- [47] J. Chen, K. Wu, H. Ma, W. Hu, and J. Yang, Tunable Rashba spin splitting in Janus transition-metal dichalcogenide monolayers via charge doping, *RSC Adv.* **10**, 6388 (2020).
- [48] Y. Hu, Y. Yin, G. Ding, J. Liu, H. Zhou, W. Feng, G. Zhang, and D. Li, High thermal conductivity in covalently bonded Bi-layer honeycomb boron arsenide, *Mater. Today Phys.* **17**, 100346 (2021).
- [49] F. Tian *et al.*, Unusual high thermal conductivity in boron arsenide bulk crystals, *Science* **361**, 582 (2018).
- [50] J. Shin, G. A. Gamage, Z. Ding, K. Chen, F. Tian, X. Qian, J. Zhou, H. Lee, J. Zhou, L. Shi, T. Nguyen, F. Han, M. Li, D. Broido, A. Schmidt, Z. Ren, and G. Chen, High ambipolar mobility in cubic boron arsenide, *Science* **377**, 437 (2022).
- [51] S. Yue, F. Tian, X. Sui, M. Mohebinia, X. Wu, T. Tong, Z. Wang, B. Wu, Q. Zhang, Z. Ren, J. Bao, and X. Liu, High ambipolar mobility in cubic boron arsenide revealed by transient reflectivity microscopy, *Science* **377**, 433 (2022).
- [52] H. Fan, H. Wu, L. Lindsay, and Y. Hu, Ab initio investigation of single-layer high thermal conductivity boron compounds, *Phys. Rev. B* **100**, 085420 (2019).
- [53] G. Kresse and J. Furthmüller, Efficient iterative schemes for ab initio total-energy calculations using a plane-wave basis set, *Phys. Rev. B* **54**, 11169 (1996).
- [54] G. Kresse and J. Furthmüller, Efficiency of ab-initio total energy calculations for metals and semiconductors using a plane-wave basis set, *Comput. Mater. Sci.* **6**, 15 (1996).
- [55] G. Kresse and D. Joubert, From ultrasoft pseudopotentials to the projector augmented-wave method, *Phys. Rev. B* **59**, 1758 (1999).
- [56] J. P. Perdew, K. Burke, and M. Ernzerhof, Generalized gradient approximation made simple, *Phys. Rev. Lett.* **77**, 3865 (1996).
- [57] H. J. Monkhorst and J. D. Pack, Special points for Brillouin-zone integrations, *Phys. Rev. B* **13**, 5188 (1976).
- [58] A. Togo, F. Oba, and I. Tanaka, First-principles calculations of the ferroelastic transition between rutile-type and CaCl₂-Type SiO₂ at high pressures, *Phys. Rev. B* **78**, 134106 (2008).
- [59] W. Li, J. Carrete, N. A. Katcho, and N. Mingo, ShengBTE: A solver of the Boltzmann transport equation for phonons, *Comput. Phys. Commun.* **185**, 1747 (2014).
- [60] See Supplemental Material at <http://link.aps.org/supplemental/10.1103/PhysRevB.109.205408> for details of the planar average of the electrostatic potential energy; magnification of phonon dispersion; AIMD simulations; phonon dispersion considering LO-TO splitting; specific electronic band-structure information; DOS of each atom under the external electric field; convergence test of cutoff radius and Q grid; temperature-dependent thermal conductivity of different phonon branches; model-level analysis of phonon group velocity and scattering phase space; charge transfer of B and As atoms.
- [61] S. Bi, Z. Chang, K. Yuan, Z. Sun, X. Zhang, Y. Gao, and D. Tang, First-principles prediction of the lattice thermal conductivity of two-dimensional (2D) h-BX (X = P, As, Sb) considering the effects of fourth-order and all-order scattering, *J. Appl. Phys.* **132**, 114301 (2022).
- [62] X.-B. Xiao, Q. Ye, Z.-F. Liu, Q.-P. Wu, Y. Li, and G.-P. Ai, Electric field controlled indirect-direct-indirect band gap transition in monolayer InSe, *Nanoscale Res. Lett.* **14**, 322 (2019).
- [63] S. Patel, U. Dey, N. P. Adhikari, and A. Taraphder, Electric field and strain-induced band-gap engineering and manipulation of the Rashba spin splitting in Janus van der Waals heterostructures, *Phys. Rev. B* **106**, 035125 (2022).
- [64] A. Ramasubramaniam, D. Naveh, and E. Towe, Tunable band gaps in bilayer transition-metal dichalcogenides, *Phys. Rev. B* **84**, 205325 (2011).
- [65] T. Ayadi, L. Debbichi, M. Badawi, M. Said, D. Rocca, and S. Lebegue, An ab initio study of the electronic properties of the ferroelectric heterostructure In₂Se₃/Bi₂Se₃, *Appl. Surf. Sci.* **538**, 148066 (2021).

- [66] H. Liu, G. Zhang, X. Zheng, F. Chen, and H. Duan, Emerging miniaturized energy storage devices for microsystem applications: From design to integration, *Int. J. Extrem. Manuf.* **2**, 042001 (2020).
- [67] H. Liu, J. Li, X. Zhang, X. Liu, Y. Yan, F. Chen, G. Zhang, and H. Duan, Ultrathin and ultralight Zn micromesh-induced spatial-selection deposition for flexible high-specific-energy Zn-ion batteries, *Adv. Funct. Mater.* **31**, 2106550 (2021).
- [68] Z. Sun, K. Yuan, Z. Chang, X. Zhang, G. Qin, and D. Tang, Efficient thermal conductivity modulation by manipulating interlayer interactions: A comparative study of bilayer graphene and graphite, *J. Appl. Phys.* **126**, 125104 (2019).
- [69] F. Duan, C. Shen, H. Zhang, and G. Qin, Hydrodynamically enhanced thermal transport due to strong interlayer interactions: A case study of strained bilayer graphene, *Phys. Rev. B* **105**, 125406 (2022).